sustainability

Article

Application of a Semi-Empirical Approach to Map Maximum Urban Heat Island Intensity in Singapore

Beatriz Sanchez [1,2,*], Matthias Roth [2], Pratiman Patel [2] and Andrés Simón-Moral [3]

1 Research Center for Energy, Environment and Technology, CIEMAT, 28040 Madrid, Spain
2 Department of Geography, National University of Singapore, Singapore 117597, Singapore; geomr@nus.edu.sg (M.R.); pratiman@nus.edu.sg (P.P.)
3 TECNALIA, Basque Research and Technology Alliance (BRTA), 48160 Derio, Spain; andres.simon@tecnalia.com
* Correspondence: beatriz.sanchez@ciemat.es

Abstract: Differences in land surface characteristics across a city produce great spatial and temporal variability in air temperature. This fact is particularly pronounced between urban and surrounding rural areas giving rise to the canopy-layer urban heat island (CL-UHI) phenomenon. In the present study, we apply the dimensional analysis technique to develop a simple semi-empirical equation to map daily maximum CL-UHI (UHI_{max}) intensities during nighttime over the city of Singapore for specific weather conditions. By adopting the methodology proposed by Theeuwes et al., but selecting meteorological and morphological parameters that affect UHI_{max} intensity most for Singapore, evaluation of the developed equation shows good agreement with observations (RMSE = 1.13 K and IOA = 0.76). Model performance depends strongly on wind conditions and is best during weak winds when 'ideal' conditions for UHI development are approached (RMSE = 0.65 K and IOA = 0.85). Results using the simple equation developed to map UHI_{max} intensities in Singapore under dry weather conditions are comparable to those obtained from more sophisticated numerical models, which demand significant computational resources, and the complex parameterizations involved require expertise to carry out the simulations. The resulting maps of the present study can be used to investigate less favorable thermal conditions and assess population vulnerability to a certain temperature excess, as well as provide insights for urban planning strategies of mitigation measures according to the land cover and morphology of a location.

Keywords: daily maximum UHI maps; dimensional analysis; simple theoretical equation; intra-urban air temperature variability; local climate zones; tropical city

Citation: Sanchez, B.; Roth, M.; Patel, P.; Simón-Moral, A. Application of a Semi-Empirical Approach to Map Maximum Urban Heat Island Intensity in Singapore. *Sustainability* **2023**, *15*, 12834. https://doi.org/10.3390/su151712834

Academic Editors: Dimitra Founda and George Katavoutas

Received: 18 June 2023
Revised: 18 August 2023
Accepted: 22 August 2023
Published: 24 August 2023

1. Introduction

The urban heat island is a well-known phenomenon that has been studied since the early 19th century [1]. Of the various heat island types, the canopy-layer urban heat island (CL-UHI) is the most important one with regard to healthy and sustainable cities. It is quantified as the difference in near-surface air temperature between built-up areas and rural surroundings [2]. Numerous studies have focused on understanding and explaining the processes involved in this phenomenon in diverse urban environments around the world [3–5]. Urban morphology, land cover, and anthropogenic heat fluxes are key factors altering the local surface energy balance, which, together with geographical location and meteorological conditions, produce nocturnal heat islands of various intensities. In particular, the prevalence of impervious as opposed to natural surfaces in the city, the presence of buildings, and the high thermal admittance of urban materials increase the absorption of incoming shortwave radiation and storage of heat energy. Moreover, the available energy is preferentially partitioned into sensible at the expense of latent heat flux. All these factors contribute to a reduced nocturnal cooling rate in the city, which gives rise to higher urban–rural air temperature differences [6]. CL-UHI magnitudes are generally negatively (positively) correlated with the sky-view factor (street aspect ratio) [7–9], inverse relationships are found with the amount of urban vegetation [10–12], and local circulations such as the sea breeze have been shown to reduce urban heat [13,14].

The CL-UHI effect has been thoroughly studied using observations [15–17] and numerical models [18,19]. Monitoring studies can be expensive and time-consuming and are often limited to a few individual sites and meteorological conditions and are therefore not necessarily representative of air temperature variability across entire cities, weather conditions, or particular seasons. Numerical models instead are capable of estimating spatiotemporal patterns of CL-UHI intensity through sophisticated simulations but are approximations of reality and need to be properly validated. Numerous studies have focused on simulating the spatial variability of CL-UHI intensities in many different cities [19–23]. Some have also assessed model sensitivity to distinct urban parameterization schemes (e.g., single or multi-layer urban canopy models) [24,25]. However, all these models demand significant computational resources, and the complex parameterizations involved require expertise to carry out the simulations. Hence, more simple approaches, such as empirical models based on observations, have been developed to estimate spatial air temperature patterns and CL-UHI intensities. The relative simplicity of this empirical approach makes it easy to use; however, the application of such a model is restricted to conditions similar to those under which it was developed, e.g., for a particular location and specific weather conditions. The most common statistical approach uses multiple linear regression relationships between the CL-UHI and parameters known to influence its intensity [26–29]. However, these models do not provide much insight into the physical workings of the phenomenon. Alternatively, some studies use physically based equations and dimensional analysis based on Buckingham's Π-theorem [30] to estimate CL-UHI patterns. This technique consists of extracting dimensionless variables based on the physical dimensions (e.g., time, mass) of physical quantities giving rise to a physically meaningful equation between independent variables. Previous studies using scaling methods have derived physically based equations to calculate CL-UHI intensities based on variables such as boundary layer height or surface sensible heat flux, which might not commonly be measured in other cities [31,32].

A more recent study by Theeuwes et al. [33] (hereafter referred to as T17) developed a diagnostic equation to calculate the nocturnal maximum CL-UHI intensity using commonly measured standard weather variables such as air temperature, radiation, and wind speed. Empirical models are usually designed for a single study city; however, T17 proved that this equation was giving good results in the 14 European cities studied. To our knowledge, at least two studies have applied the equation developed by T17 in Chinese cities. Results from the humid subtropical city of Xi'an [34] and the temperate climate city of Nanjing [35,36] show reasonable agreement with observations, although model–observation correlations were slightly worse than those obtained by T17. Hence, Zhang et al. [34] adapted the original equation to the target city in order to better represent the local characteristics.

The main objective of the present study is to develop a simple semi-empirical equation using basic climate and urban land cover parameters to estimate daily maximum CL-UHI intensity (UHI_{max}) using long-term observations in tropical Singapore. To achieve this purpose, we adapt the methodology proposed in T17 to better represent the local characteristics of Singapore. A number of past studies have already analyzed the spatial and temporal evolution of CL-UHI intensity over Singapore using observations [37–39] and numerical simulations [40]. However, the present study provides an alternative method to estimate spatial patterns of maximum CL-UHI intensities that is easy to apply and provides detailed spatial information on the local-scale air temperature variability under selected meteorological conditions. Section 2 provides a description of the study area, observation network, local climate, and urban morphological characteristics of Singapore. The original T17 model is applied to Singapore in Section 3. Section 4 introduces the modified model for Singapore, which is evaluated in Section 5. Maps of UHI_{max} intensities for different weather conditions are shown in Section 6, followed by a discussion and concluding remarks in Section 7.

2. Study Area, Observational Data, and Urban Morphological Characteristics

Singapore is an island city-state located close to the equator (1°21′ N, 103°49′ E) occupying an area of ∼722.5 km^2 [41] (Figure 1). Most of the terrain is low-lying with little change in topography across the island. The highest point is 168 m a.s.l., located in a nature reserve close to the center of the island, which is also home to several freshwater reservoirs. Regarding land cover classification, the local climate zone (LCZ) scheme is sometimes used to divide the landscape into regions of uniform surface cover, structure, material, and human activity, having a characteristic CL air temperature [42]. The LCZ map for Singapore is developed using Google Earth Engine, a cloud-based platform for planetary-scale geospatial analysis [43,44]. The procedure consists of classifying several times the training areas developed for Singapore into LCZ categories, using satellite data products within the period 2014–2016, and the final LCZ map comprises the modal category [45]. The most predominant built type region in Singapore is LCZ 4 (open high-rise), followed by LCZs 9 (sparsely built) and 8 (large low-rise), respectively (Figure 1, [45]).

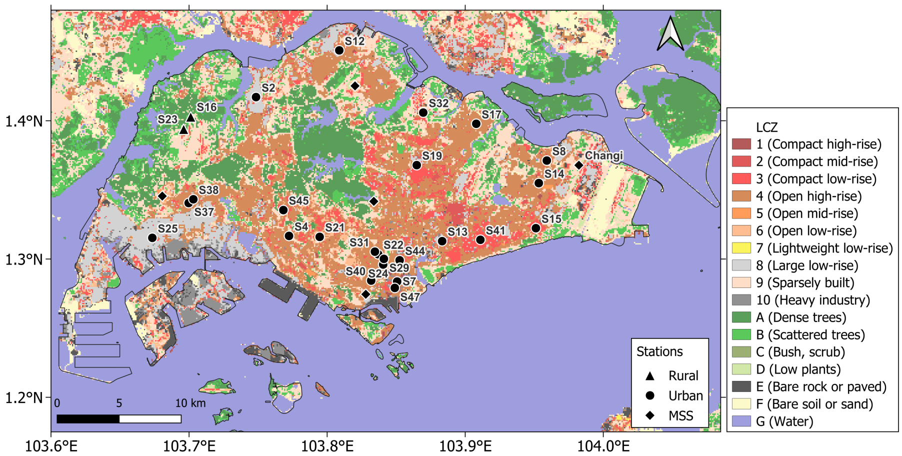

Figure 1. Location of five MSS weather stations (diamond) and 26 air temperature sensors at 2–3 m height, of which 24 are placed in urban areas (dots) and two in rural areas with scattered trees (triangle). Background image: LCZ map from Middel et al. [45].

Observations obtained between August 2011 and May 2014 are used in the present study with experimental details fully explained in Roth et al. [39] (referred to as R22 hereafter). Briefly, a network of sensors installed specifically to measure air temperature at a height of 2–3 m above ground provides locally representative observations. Twenty-four sensors are located in urban areas and two in rural areas representing the rural 'reference' (Figure 1). Sensor locations were chosen to represent maximum thermal differences between neighborhoods representing a wide range of LCZ classes found in Singapore. Relevant key features of the 26 stations used are summarized in Table 1, which lists station coordinates and the morphological and land cover characteristics within a 300 m grid covering the respective station. Except for the local sky-view factor (SVF), which is obtained at the actual station location, urban parameters represent average values across a 300 m × 300 m grid cell closest to the station used in a recent numerical modeling study [46]. Also, 300 m × 300 m corresponds to the footprint or source areas of canopy-layer air temperature sensors (see, e.g., [39]). Data from an additional five weather stations operated by the Meteorological Service of Singapore (MSS) are employed to select days without rainfall (Figure 1). Finally, synoptic weather conditions are characterized using solar radiation, 2 m air and dew-point temperatures, and 10 m wind speed collected at the MSS Changi weather station (Figure 1).

Daily UHI$_{\max}$ magnitude is computed as the maximum difference of hourly air temperature at any urban station ($T_{2m,urb}$) minus the air temperature at the rural reference station ($T_{2m,rur}$) during nighttime (from 20 LT to 06 LT): UHI$_{\max}$ = $T_{2m,urb} - T_{2m,rur}$. Here, $T_{2m,rur}$ is calculated as the average of stations S16 and S23 (see R22 for further explanations on the selection of the rural reference sites). R22 presents a detailed analysis of the effect of weather on CL-UHI, with the highest magnitudes observed during dry, calm, and clear nights. Using the same filtering approach for 'ideal' conditions as in R22 leaves only 36 nights or 3.5% of the entire dataset. This sample size is too small for rigorous analysis. Hence, the present study only filters for rainfall by excluding days with >0.2 mm rainfall measured simultaneously at the five MSS stations. The remaining dataset for further analysis comprises 303 dry days (30% of the original data).

Table 1. Coordinates, morphological and land cover characteristics of measurement stations. SVF—sky-view factor, H/W—height-to-width ratio, F_{urb}—urban fraction, F_{veg}—vegetation fraction, LCZ—local climate zone. LCZ 1 (compact high-rise), LCZ 2 (compact midrise), LCZ 3 (compact low-rise), LCZ 4 (open high-rise), LCZ 5 (open midrise), LCZ 6 (open low-rise), LCZ 8 (large low-rise), LCZ A (dense trees), and LCZ B (scattered trees) [42].

Station ID	Lon (°)	Lat (°)	Local SVF	H/W (300-m Average)	F_{urb} (300-m Average)	F_{veg} (300-m Average)	LCZ
Urban stations							
S2	1.4171	103.7485	0.69	0.41	0.88	0.10	8
S4	1.3167	103.7724	0.19	0.20	0.44	0.47	A/4
S7	1.2837	103.8507	0.19	5.16	0.87	0.06	1
S8	1.3712	103.9591	0.37	0.97	0.64	0.31	4
S12	1.4509	103.8088	0.55	0.44	0.85	0.10	8
S13	1.3129	103.8833	0.66	0.96	0.84	0.13	2
S14	1.3549	103.9533	0.32	0.94	0.76	0.19	4
S15	1.3223	103.9512	0.67	0.76	0.75	0.20	3
S17	1.3978	103.9080	0.47	1.83	0.77	0.20	4
S19	1.3679	103.8649	0.84	0.77	0.76	0.19	3
S21	1.3160	103.7946	0.54	0.61	0.43	0.56	6
S22	1.3035	103.8369	0.24	2.49	0.82	0.17	1
S24	1.2960	103.8406	0.55	1.52	0.68	0.30	5
S25	1.3153	103.6734	0.56	0.39	0.90	0.07	8
S29	1.3001	103.8411	0.52	1.18	0.69	0.30	4
S31	1.3053	103.8346	0.70	2.15	0.82	0.17	3
S32	1.4059	103.8696	0.78	0.14	0.30	0.70	6
S37	1.3405	103.6997	0.70	0.99	0.70	0.25	4
S38	1.3432	103.7031	0.26	1.52	0.69	0.28	4
S40	1.2844	103.8319	0.44	0.63	0.70	0.28	5
S41	1.3139	103.9110	0.86	0.88	0.78	0.18	3
S44	1.2991	103.8525	0.41	1.84	0.91	0.09	1/2
S45	1.3354	103.7683	0.79	0.74	0.76	0.24	3
S47	1.2791	103.8490	0.14	3.81	0.91	0.09	1
Rural stations [1]							
S16	1.4028	103.7012	0.66	0.01	0.08	0.9	B
S23	1.3939	103.6961	0.83	0.01	0.07	0.9	B

[1] Air temperatures from S16 and S23 are averaged to calculate the rural reference air temperature.

3. Application of Diagnostic Equation Proposed in Theeuwes et al. [33]

Below we apply the diagnostic equation proposed by T17 and evaluate its performance in the context of tropical Singapore. T17 derives the following relationship based on dimensional analysis and using routine weather observations and standard land cover and morphological parameters:

$$\mathrm{UHI}_{\max} = (2 - SVF - F_{veg})\sqrt[4]{\frac{K_{in} \cdot DTR^3}{U_{24h,av}}} \tag{1}$$

Here, K_{in} is the downward shortwave radiation in kinematic units (K m s^{-1})), DTR the daily temperature range (DTR (K) = $T_{max} - T_{min}$), and $U_{24h,av}$ the 24 h average 10 m wind speed (m s^{-1}), all measured at a rural reference site. The SVF at the station location is estimated from building height and street width data, and F_{veg} is the vegetation fraction within a 500 m circle centered on the urban station. Equation (1) is only valid over the parameter range for which it has been developed, which for SVF and F_{veg} are 0.2 to 0.9 and 0 to 0.4, respectively. Hence, our stations S4, S7, S21, S32, and S47 are excluded from the evaluation. Also, since the present study did not measure K_{in} and $U_{24h,av}$ at our rural sites, we use respective data from the Changi weather station (Figure 1). Given that Changi is an official WMO weather station (WMO Index Number: 48698) and considering the absence of significant topography and little variability of synoptic conditions across the relatively small size of Singapore, we assume that the Changi data is representative of regional weather and hence similar day-to-day variability is expected to that at the rural sites. Therefore, using K_{in} and $U_{24h,av}$ at Changi station, DTR measured at the rural site and SVF, and F_{veg} from Table 1, the proposed equation in T17 (Equation (1)) is applied to predict UHI_{max} intensities at 19 urban stations for the 303 dry days of the study period. Modeled UHI_{max} magnitudes are compared with observed UHI_{max} intensities at the selected urban stations (Figure 2a).

Model accuracy is quantified using the index of agreement (IOA) and Pearson correlation coefficient (R), and the root mean squared error (RMSE) and median absolute error (MEAE) are used to calculate model deviations from observations. Although the errors appear acceptable (RMSE = 1.10 K and MEAE = 0.75 K), UHI_{max} is slightly overestimated, and the relationships show considerable scatter (Figure 2a).

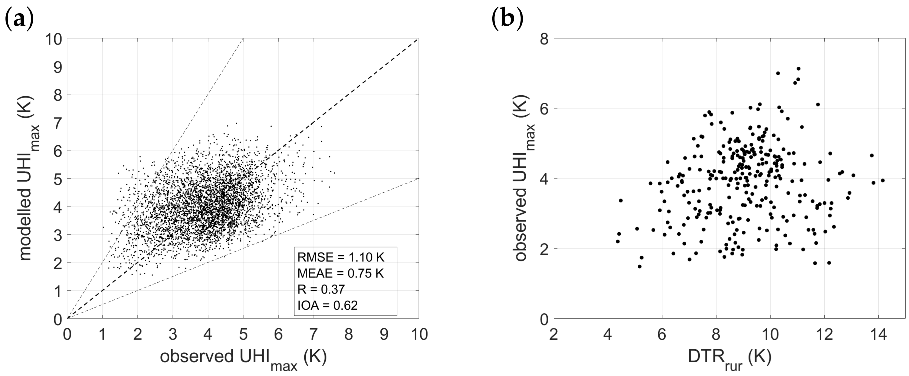

Figure 2. (**a**) Modeled UHI_{max} applying Equation (1) against observed UHI_{max} from 19 urban stations for dry days. (**b**) Relationship between observed UHI_{max} and DTR_{rur} at Station S41 for dry days.

Compared to previous studies using the same approach, model error statistics are similar to those obtained for European cities (RMSE = 0.91 K and MEAE = 0.58 K) (T17) or Nanjing (RMSE = 1.00 K and MEAE = 0.68 K) [36]. However, the present R value is significantly lower, 0.37, compared to 0.81 and 0.67, respectively. The poor performance of the model for Singapore is hypothesized to be due to a combination of reasons:

- Different reference stations are used for the weather variables. K_{in} and $U_{24h,av}$ are mainly considered in the equation to determine the seasonal variability of weather conditions within the study period. Although similar day-to-day variability is expected at Changi compared to the rural site, the magnitude, particularly for wind speed, might vary.
- The rural reference sites are characterized by different land cover types. LCZ D (low plants) is used in T17, but LCZ B (scattered trees) in the present study. DTR for the former is therefore likely larger since daytime air temperature will be higher over an open area, compared to a partially shaded area. This discrepancy could be responsible for the large scatter in Figure 2b, as compared to the strong relationship between UHI_{max} and DTR observed in T17.

Although model errors are comparable to those obtained in other cities, empirical equations are restricted to circumstances similar to those under which they were derived. The established ranges for urban parameters (SVF and F_{veg}) also exclude some stations representative of specific areas of Singapore (e.g., S7 (LCZ 1) in the business district). Given the important differences in the local climate context, we therefore develop in the next section a similar equation following the same methodology proposed by T17, but selecting meteorological and morphological parameters that provide better explanatory power for UHI_{max} intensities for the specific local climate and urban geometry of Singapore.

4. Development of the Model Equation for Singapore

The empirical equation developed here is based on relationships between independent variables thought to significantly affect UHI_{max} intensities. A set of dimensionless groups is defined from such variables through dimensionless analysis [30], from which a relationship with UHI_{max} is determined empirically using data from 24 urban stations and 303 dry days.

4.1. Selection of Independent Variables

4.1.1. Land Cover and Morphological Parameters

Land cover and morphological parameters are key factors in generating nighttime intra-urban differences in air temperature and hence CL-UHI magnitude [2]. As expected, UHI_{max} increases with urban fraction (F_{urb}) and decreases with F_{veg}, with a slightly lower correlation coefficient for the latter (Figure 3). Street geometry can be characterized by street aspect ratio (H/W) and SVF. In the present study, H/W is the average for an area within a 300 m circle centered on the station, and SVF is determined from fisheye images at the actual station location [47]. Scatter plots do not reveal a clear trend of UHI_{max} with the local SVF (R = 0.13, Figure 3d). On the other hand, a good fit in the form of an exponential relationship is found for H/W (R = 0.77, Figure 3c). Therefore, F_{urb} and H/W are selected as key independent variables to build our model.

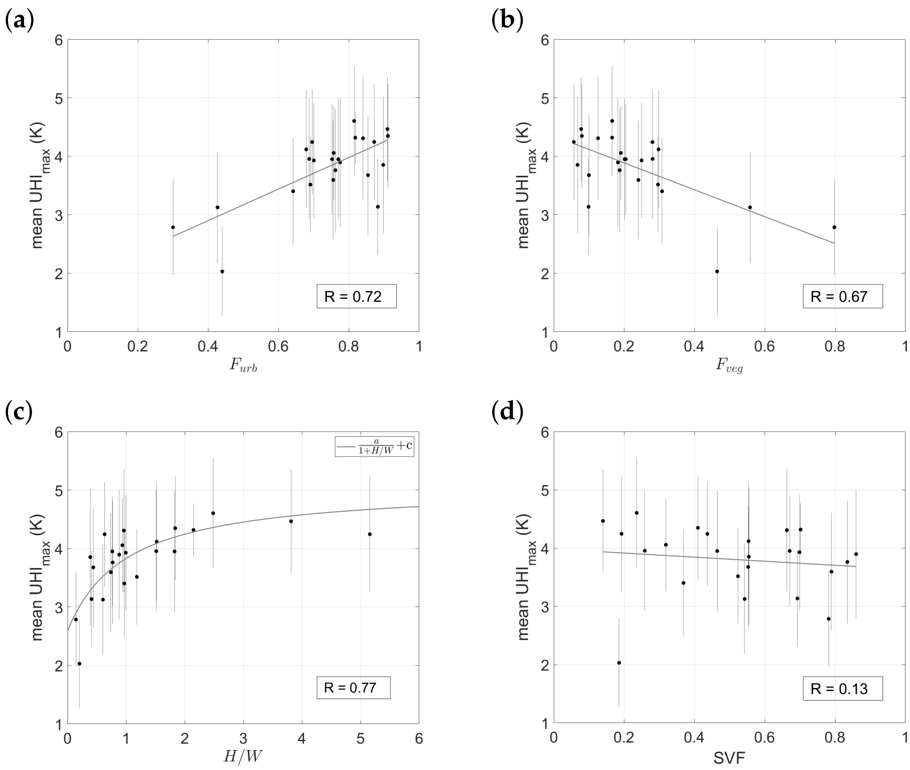

Figure 3. Observed mean UHI_{max} at 24 urban stations for dry days against: (**a**) urban fraction (F_{urb}), (**b**) vegetation fraction (F_{veg}), (**c**) street aspect ratio (H/W) and (**d**) local sky-view factor (SVF). Vertical lines denote +/−1 standard deviation.

4.1.2. Meteorological Variables

Meteorological conditions influence UHI development and are therefore important to determine urban–rural differences [2,39]. Here, we select representative meteorological variables that are known to affect daily and seasonal UHI_{max} intensity.

Wind limits the development of the CL-UHI, the latter being largest under calm conditions [39,48]. Wind speed measured at 10 m a.g.l. (U_{ref}) is chosen as one of the key variables in the model. In addition, clear skies promote strong daytime insolation and larger nighttime UHI intensity given that surface cooling driven by longwave radiation loss is slower in urban than rural environments. Incoming shortwave radiation (K_{in}) reflects the day-to-day variability of the energy that reaches the urban surface and hence can be used as a proxy of daytime cloud conditions, with the assumption that similar conditions extend into nighttime.

Soil moisture also contributes to CL-UHI development and variability (e.g., [49]). Wet rural soils will have a higher heat capacity (and thermal admittance) and hence slow nighttime cooling, which will result in a reduced UHI intensity. To some extent, this variable is already considered by selecting dry days only. However, soil moisture also varies within dry days depending on how much time has passed since a particular rainfall event. The proposed model also considers a reference air ($T_{a,ref}$) and dew-point ($T_{d,ref}$) temperature measured at Changi station. The ratio between $T_{a,ref}$ and $T_{d,ref}$ is an indirect measure of relative humidity and can be used to detect changes in atmospheric humidity due to short-term rainfall events as well as seasonal rainfall variability throughout the year. A positive trend is observed between UHI_{max} and $T_{a,ref}$ and $T_{d,ref}$ (Figure 4a), except for the highest magnitudes (UHI_{max} > 6 K). The reason for this is that UHI_{max} is at the time also affected by other meteorological variables and hence the difficulty to find an individual relationship with only one parameter. The scatter points with the highest UHI_{max} intensities in Figure 4a occur for high $T_{a,ref}$ but low $T_{d,ref}$, which would indicate air humidity diminishes, and it also coincides with low wind speed conditions (U_{ref} < 1.5 m s^{-1}) (Figure 4b). We therefore use $T_{a,ref}$, $T_{d,ref}$, U_{ref}, and K_{in} as indicators of further weather variability within the 303 dry days selected.

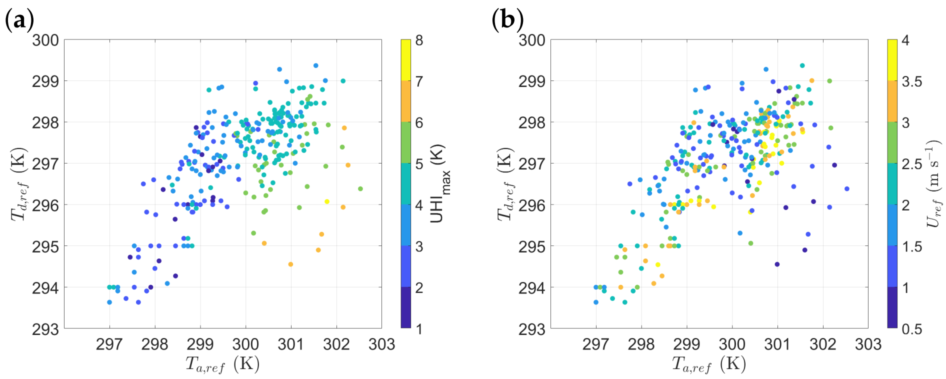

Figure 4. Relationship between: (**a**) UHI_{max} (K), $T_{a,ref}$ (K), and $T_{d,ref}$ (K), and (**b**) $T_{a,ref}$ (K), $T_{d,ref}$ (K) and U_{ref} (m s^{-1}) for S41 for dry days.

4.2. Development of the Model Equation for Singapore

To develop the equation, the dataset is randomly split into two subsets: 70% (212 nights) of the data are used to build the model and 30% (91 nights) to evaluate model performance. More data are employed to design the model to ensure the inclusion of greater variability of weather conditions. From above, the selected meteorological variables are K_{in} in its kinematic form (K m s^{-1}), nocturnal U_{ref} (m s^{-1}), $T_{a,ref}$ and $T_{d,ref}$ (K) measured at the reference Changi station, as well as land cover and morphological characteristics F_{urb} and H/W, respectively.

Given that F_{urb} and H/W are dimensionless, dimensional analysis is only applied to the meteorological variables, with the primary dimensions being temperature, length, and time. The application of Buckingham's Π-theorem (Appendix A) results in two independent dimensionless groups,

$$\Pi_1 = \frac{\mathrm{UHI_{max}}}{T_{a,ref}}; \quad \Pi_2 = \frac{K_\downarrow}{T_{d,ref} \cdot U_{ref}} \tag{2}$$

The function relating Π_1 and Π_2 is derived from observations such that $\Pi_1 = f(\Pi_2)$. Considering that f might have a linear or exponential form, $\Pi_1 = \alpha\Pi_2^{\beta}$. The latter is written as $log(\Pi_1) = \beta \cdot log(\Pi_2) + log(\alpha)$ to find the best linear fit for each station (Figure 5).

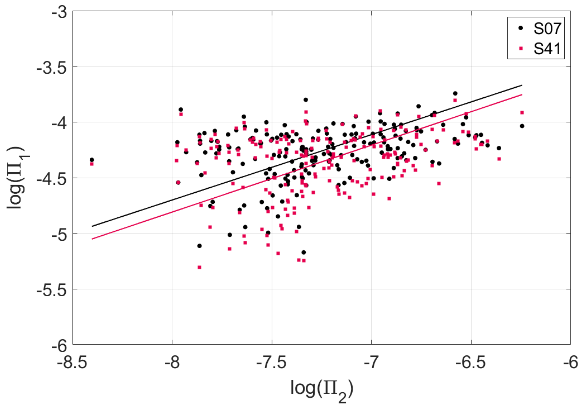

Figure 5. Relationship between the two dimensionless groups plotted as log(Π_2) against log(Π_1) for two examples, stations S07 (black) and S41 (red) and the respective linear trend lines.

The linear fit for each station provides the best fit with a slope of β = 0.6 (3/5) for all stations. Hence, the relationship between Π_1 and Π_2 can be written as $\Pi_1 = \alpha_i \Pi_2^{(3/5)}$, where subscript i refers to each individual station. Unlike β, parameter α varies from station to station as a function of land cover and morphological characteristics: $\alpha = f(F_{urb}, H/W)$. The dependency on H/W is reformulated as $1 - 1/(1 + H/W)$ to obtain a positive linear trend and avoid undefined results when H/W = 0. Scatter plots between α and the morphological characteristics, F_{urb} and H/W, for all stations, show linear trends with reasonably high correlation coefficients of R = 0.72 and R = 0.76, respectively (Figure 6a,b). Hence, α can be estimated as $\alpha = a \cdot F_{urb} + b \cdot (1 - 1/(1 + H/W))$, where coefficients a and b are determined using a simple regression model to arrive at $\alpha = 0.9 \cdot F_{urb} + 0.5 \cdot (1 - 1/(1 + H/W))$ (Figure 6c).

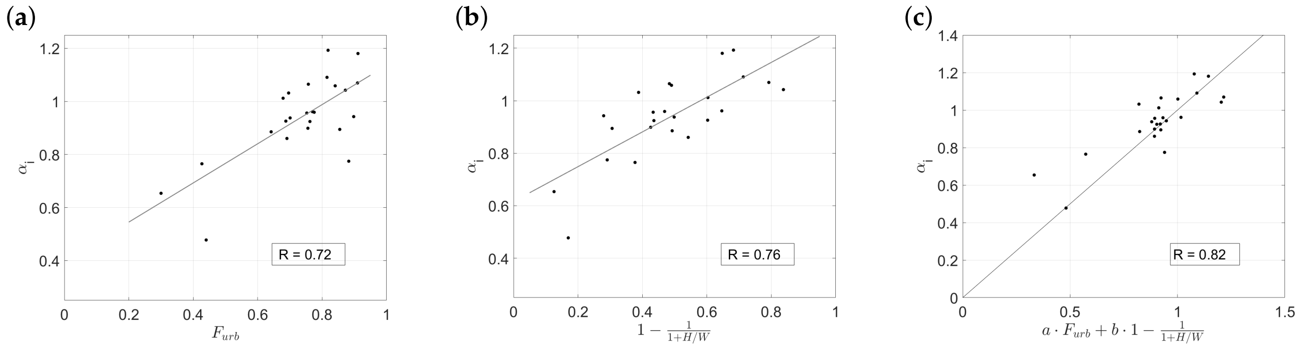

Figure 6. Scatter plots of the estimated α for each station i (α_i) against (**a**) F_{urb}, (**b**) $1 - 1/(1 + H/W)$, and (**c**) the function $a \cdot F_{urb} + b \cdot (1 - 1/(1 + H/W))$, where a and b are obtained using the multiple linear regression method and are 0.9 and 0.5, respectively.

Replacing the latter expression and rewriting the two dimensionless groups (Π_1 and Π_2) as $\Pi_1 = \alpha_i \Pi_2^{3/5}$, the final equation to estimate $\mathrm{UHI_{max}}$ magnitudes over Singapore becomes:

$$\mathrm{UHI_{max}} = \left[0.9 \cdot F_{urb} + 0.5 \cdot \left(1 - \frac{1}{1 + H/W}\right)\right] \cdot \left(\frac{T_{a,ref}^{5/3} \cdot K_{in}}{T_{d,ref} \cdot U_{ref}}\right)^{3/5} \quad (3)$$

5. Model Evaluation

The performance of Equation (3) is evaluated with the observed $\mathrm{UHI_{max}}$ using the test dataset (Figure 7). Model results show an acceptable agreement with observations (IOA = 0.76) and R = 0.58 (Figure 7) and slightly improve compared to applying the model equation (Equation (1)) proposed by T17 (Figure 2). Overall, the model slightly underestimates observed $\mathrm{UHI_{max}}$ and error metrics are similar to those observed in other studies using Equation (1) (Table 2).

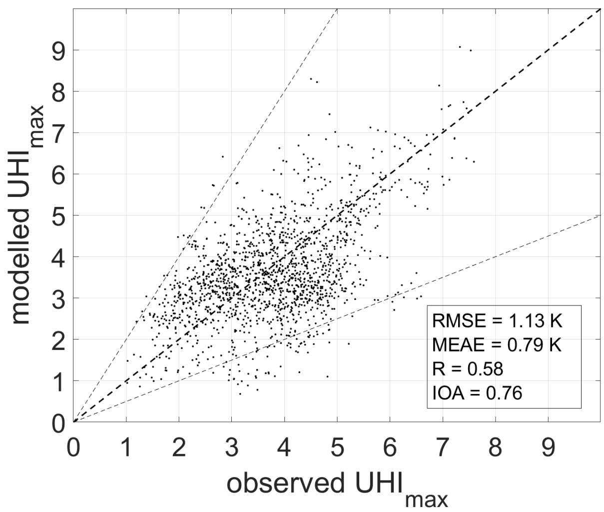

Figure 7. Modeled (using Equation (3)) against observed $\mathrm{UHI_{max}}$ for 24 stations and for the second subset of the data (91 nights). Dashed lines indicate the 1:1 relationship and the range of factor of two (FAC2).

Table 2. Model performance metrics to estimate $\mathrm{UHI_{max}}$.

Dataset	IOA	RMSE (K)	MEAE (K)	R
Theeuwes et al. [33]—European cities		0.91	0.58	0.81
Zhang et al. [34]—Xi'an (China)		1.68	1.14	0.67
Yang et al. [36]—Nanjing (China)		1.00	0.68	
Theeuwes et al. [33]—Singapore	0.62	1.10	0.75	0.37
Equation (3) for Singapore	0.76	1.13	0.79	0.58

Using the same dataset, we also analyze model performance at selected individual stations representing the range of urban LCZs present in the study area (Figure 8). Values of RMSE range between 0.9 and 1.3 K, being of the same order of magnitude as those obtained using physically based mesoscale models applied over the same study area [46,50]. The statistical model captures $\mathrm{UHI_{max}}$ variability across the selected stations with IOA varying between 0.59 and 0.76. The worst model agreement is obtained at S21 (LCZ 6). This is likely due to the low number of data points at the low end of F_{urb}, since only three urban stations have F_{urb} below 0.45.

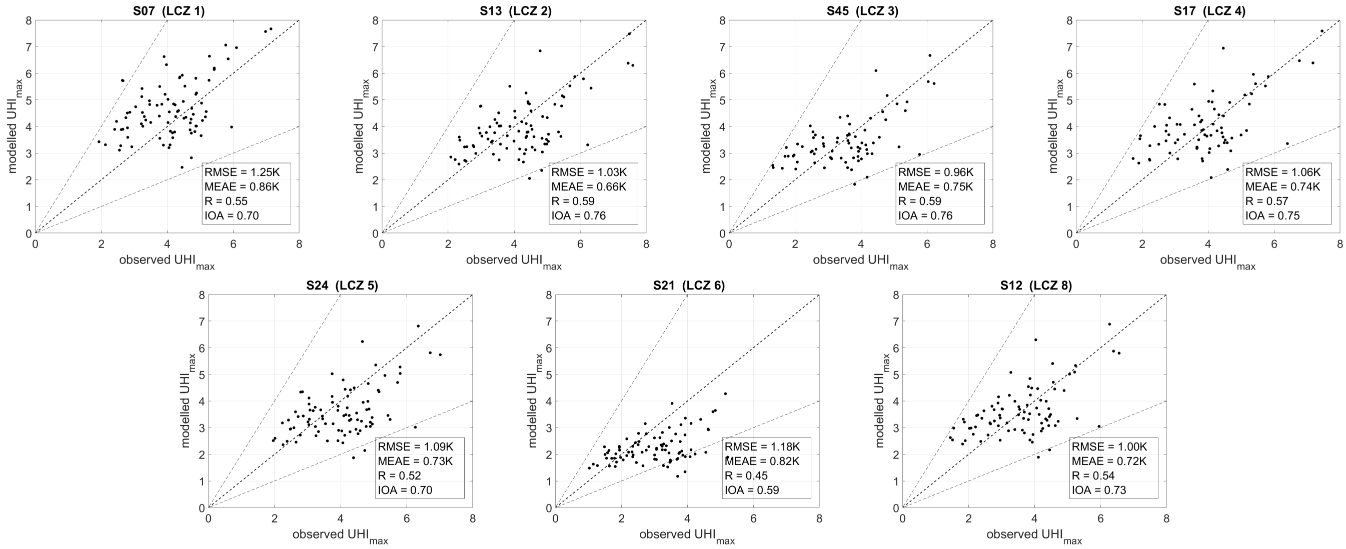

Figure 8. Same as Figure 7 for S07 (LCZ 1), S13 (LCZ 2), S45 (LCZ 3), S17 (LCZ 4), S24 (LCZ 5), S21 (LCZ 6), and S25 (LCZ 8).

Figure 8 also shows the capability of the model to estimate the variability of $\mathrm{UHI}_{\mathrm{max}}$ as a function of weather conditions variability. Further analysis at the individual station level reveals that scatter increases with stronger reference wind speed (not shown). Hence, further analysis is conducted to quantify model accuracy as a function of U_{ref} (Figure 9). Absolute errors calculated as the difference between modeled and observed $\mathrm{UHI}_{\mathrm{max}}$ magnitudes for all stations confirm that the smallest differences (<1 K) are usually found when U_{ref} is <2.5 m s^{-1} (Figure 9). Equation (3) is mainly developed to estimate $\mathrm{UHI}_{\mathrm{max}}$ intensities according to urban parameters, whose influence on UHI development is most pronounced under calm wind conditions. The best performance of the model is therefore obtained for low reference wind speeds (Table 3), which correspond to the largest $\mathrm{UHI}_{\mathrm{max}}$ values and maximum influence from local characteristics (e.g., H/W and F_{urb}).

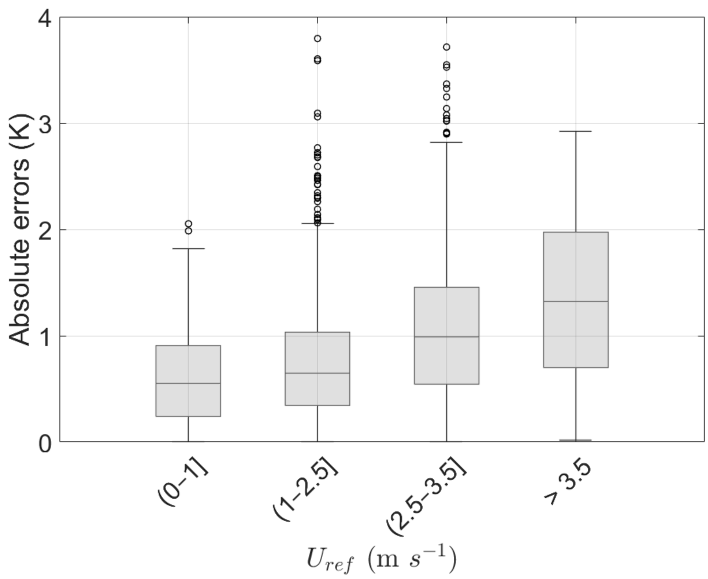

Figure 9. Absolute errors in $\mathrm{UHI}_{\mathrm{max}}$ (= $|\mathrm{UHI}_{\mathrm{max,modeled}} - \mathrm{UHI}_{\mathrm{max,observed}}|$) as a function of reference wind speed regime for the test dataset (91 nights). The box defines the interquartile range (IQR), the horizontal line is the median, whiskers extend to 1.5 times the IQR, and circles are outliers.

Table 3. Model performance metrics using the test dataset (91 nights) and entire period (303 nights) for two wind speed regimes.

Wind Speed Ranges	Test Period				Entire Period			
	IOA	**R**	**RMSE**	**MEAE**	**IOA**	**R**	**RMSE**	**MEAE**
$U_{ref} < 2.5$ m s^{-1}	0.86	0.76	0.95	0.64	0.81	0.66	0.99	0.68
$U_{ref} > 2.5$ m s^{-1}	0.49	0.31	1.33	1.03	0.70	0.50	1.18	0.84

6. Mapping Spatial Patterns of UHI_{max} Intensities

Using morphological data available for the entire city at 300 m × 300 m resolution [46], the model can be applied to generate maps of UHI_{max} intensity under dry conditions for different seasons. Figure 10 shows the spatial distribution of UHI_{max} calculated as the mean of 36 'ideal' (dry, calm, and clear) nights within the study period. The corresponding scatter plot reveals a very good correlation with observations (R = 0.85) and low prediction errors (RMSE = 0.65 K and MEAE = 0.55 K) (Table 4). These evaluation metrics confirm the better performance of the model during low wind conditions, which coincides with the maximum UHI_{max} intensity (Figure 10b).

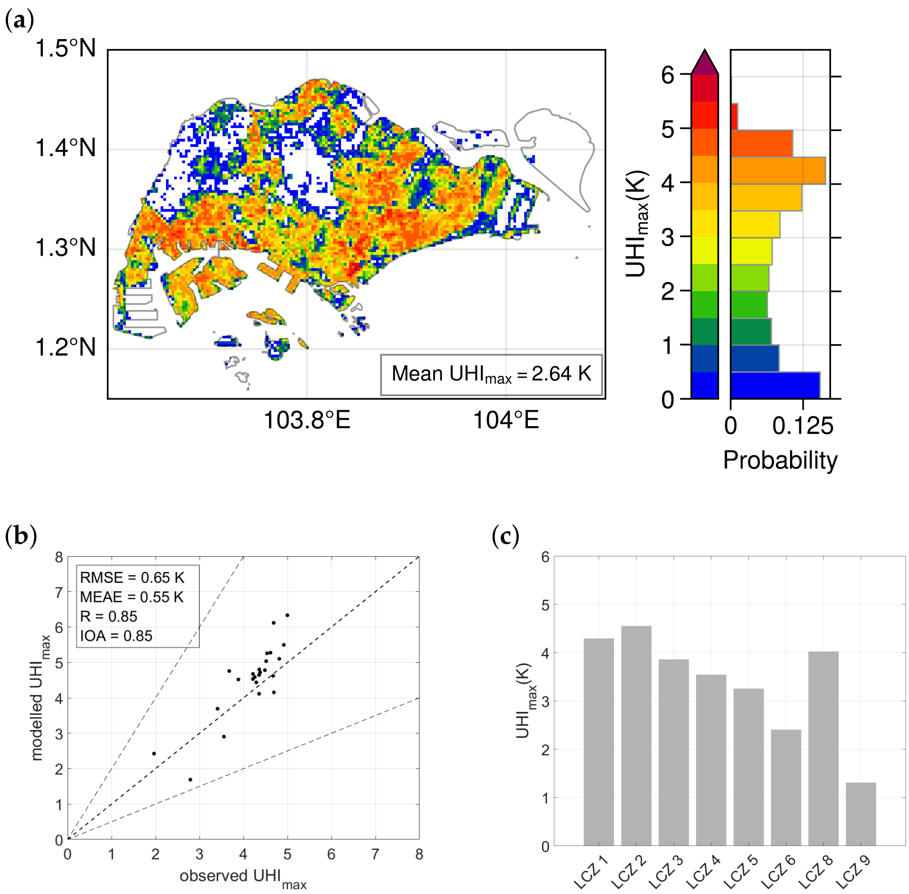

Figure 10. (**a**) Mean UHI_{max} map using Equation (3) applied to 300 m gridded morphological data for ideal conditions (36 nights), (**b**) scatter plot of modeled and observed mean UHI_{max} for the 24 urban stations, and (**c**) spatial average of modeled mean UHI_{max} for ideal nights according to the urban LCZ types.

The largest UHI_{max} intensities reach 5.5–6.0 K covering around 1% of the total area and are mainly located in the densely built-up financial and business districts (LCZ 1) close to the south-central coast. Other areas with $UHI_{max} > 4.5$ K can be found in high-density residential districts (LCZ 2) in the southeast and industrial areas (LCZ 8) in the southwest of Singapore. The spatial average of the modeled UHI_{max} across built-up areas is 2.64 K, which can be interpreted as the maximum nighttime city-wide average air temperature increment caused by the presence of the city. The most frequent UHI_{max} intensity range across the city is between 4.0 and 4.5 K, covering 16.4% of the urban area. The second most frequent range of 0.0–0.5 K covers 15.4% of the built-up area and is found next to the coast or bordering reservoirs, parks, and secondary rainforests. In addition, the gridded model results for the mean UHI_{max} are used to analyze the spatial distribution based on the urban LCZ classification by resampling the original (100 m) map [45] to the present 300 m resolution (Figure 10c). The highest UHI_{max} intensities are found in LCZs 2 and 1, with the highest magnitude of 6.1 K corresponding to a grid cell pixel located in the business district belonging to LCZ 1. The distribution of the spatial analysis follows the expected variability of urban–rural differences as a function of the LCZ class [42]. The present results are similar to those observed in previous studies in Singapore under 'ideal' heat island conditions [37,39] and support the utility of the present simple statistical modeling approach.

Additional maps represent the typical seasonal variability in Singapore (Figure 11). They include monthly average maps based on dry days for the entire study period corresponding to the month with the generally lowest and highest UHI magnitudes in February and June, respectively [37,39]. Also shown are the maps for two individual nights with the lowest and highest daily UHI_{max} observed across all stations during the study period. UHI_{max} variability across the city is low on 5 February 2012, with the most frequent UHI_{max} magnitude band of 2.0–2.5 K covering 25.7% of the total built-up area (Figure 11a). Maximum values barely exceed 3.0 K (0.3% of the area), and the average nighttime temperature increment due to built-up areas across the city is 1.49 K. Comparison with observations shows good model performance (Table 4). February is part of the Northeast monsoon season and characterized by cloudy and rainy conditions, but the model nevertheless works well for dry periods during this otherwise wet month.

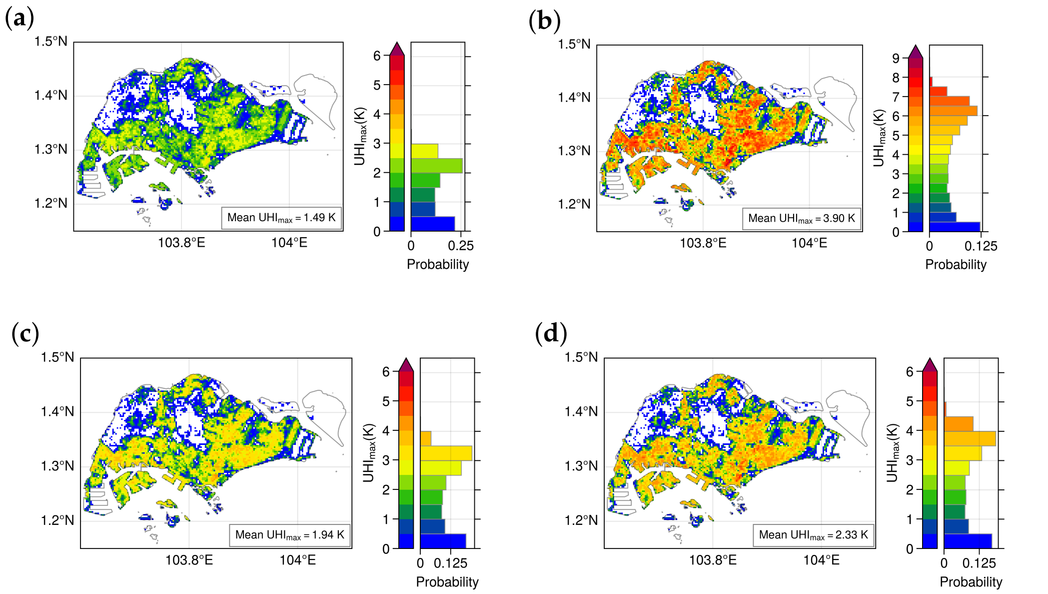

Figure 11. Maps for the (**a**) lowest UHI_{max} intensity observed on 5 February 2012, (**b**) highest UHI_{max} observed on 19 June 2013, (**c**) mean UHI_{max} map for dry days in February, and (**d**) mean UHI_{max} map for dry days in June within the study period.

Spatial UHI_{max} variability is much larger when values are higher, as shown by the map for 19 June 2013 (Figure 11b). Five stations recorded their highest UHI_{max} intensity on this day, with the highest value of 7.53 K observed at S07 (LCZ 1) [39]. June coincides with the inter-monsoon period, which is characterized by calm winds and clear skies, both of which maximize heat island development and hence differences across different land covers. Unlike for February, the UHI_{max} probability distribution shows larger magnitudes and hence larger differences across different urban areas. The most prevalent UHI_{max} temperature bin is 6.0–6.5 K and covers 11.6% of the built-up area. Maximum intensities reach between 8.0 and 8.5 K. This is slightly higher than what was observed, but this particular range is only modeled over 0.1% of the built-up area, and 5% of the area shows UHI_{max} values > 7.0 K as observed at five stations. This confirms that the model is able to accurately capture the peak UHI_{max} values during these conditions. Model error metrics more generally also suggest good performance for this particular day (Table 4). The available spatial data also enable predicting the area (and population) exposed to a certain urban temperature excess, an important measure related to human thermal comfort. In the case of this particular day, 50% of the city's built-up area, for example, was experiencing an UHI_{max} of 4.5 K or higher.

The corresponding monthly average maps confirm the generally lower (larger) UHI_{max} values and variability across the city experienced in February (June) (Figure 11c,d), as a result of the particular weather conditions in each month pointed out above. The spatial distribution is similar in both months, with the highest and lowest UHI_{max} values obtained over the more heavily built-up and greener areas, respectively. The maximum February (June) UHI_{max} values do not exceed 4.0 (5.0) K, and the probability distribution peaks between 3.0 and 3.5 (3.5–4.0) K, with ∼50% of the built-up area experiencing UHI_{max} values > 2.0 (2.5) K. Highest values always correspond to the south-central coast classified as LCZ 1. The mean UHI max across all built-up areas in February (June) is 1.94 (2.33) K. The model evaluated across all days of the respective month shows again good performance with a high R of 0.83 and prediction errors of between 0.52 and 1.01 K (Table 4).

Table 4. Model performance metrics for different periods and weather conditions.

Case	IOA	R	RMSE (K)	MEAE (K)
'Ideal' conditions	0.85	0.85	0.65	0.55
Lowest UHI_{max}—5 February 2012	0.55	0.80	0.94	0.84
Largest UHI_{max}—19 June 2013	0.89	0.86	0.90	0.52
mean UHI_{max} for February	0.82	0.83	0.57	0.55
mean UHI_{max} for June	0.72	0.83	1.01	0.90

7. Summary and Conclusions

A semi-empirical equation is derived to estimate daily UHI_{max} intensities in Singapore using the dimensional analysis technique and long-term (∼3 years) observations. The main purpose is to generate a simple and fast method to map the spatial distribution of UHI_{max} for dry weather conditions based on F_{urb} and H/W.

We first tested the equation proposed by T17 for European cities for Singapore using the available weather data. The comparison of the model with observations results in slightly higher prediction errors but relatively low agreement compared to those obtained in T17. This discrepancy is hypothesized to be partly due to the present weather reference values (K_{in} and U_{ref}) not being obtained at the rural reference site, but rather an official weather station. A more important reason for the differences is, however, the choice of the rural reference site which is grass and cropland in T17, but scattered trees in the present study. This will influence the cooling behavior of the rural environment and therefore alter the relationship between UHI_{max} and DTR [33]. We therefore develop a similar statistical model but adapted to predict UHI_{max} intensities during dry conditions in Singapore using the methodology proposed in T17. The main results are as follows:

- Evaluation of the model adapted to Singapore (Equation (3)) shows overall good agreement with observations of daily UHI_{max} for different dry weather conditions.
- Model performance shows a strong dependency of the estimated UHI_{max} on wind speed. Best performance is reached for low wind speed (<2.5 m s^{-1} at the reference

site). During these conditions, the model provides reliable estimations of UHI_{max} with low errors (RMSE and MEAE < 1 K) and a high level of agreement with observations (R > 0.80).

- Estimates for UHI_{max} tend to underpredict observed values over open low-rise areas (LCZ 6) (R < 0.5). The paucity of stations with low F_{urb} values (0.3–0.6), compared to the majority of stations that are placed in more densely built-up environments (F_{urb} > 0.6), is one reason why the model is less robust over these open urban landscapes. Given nevertheless significant UHI_{max} magnitudes over less developed urban spaces, we suggest increasing the placement of stations in these areas.
- The low prediction errors (RMSE < 1.2 K and MEAE < 1 K) obtained at every station and for different seasons in Singapore reveal that the accuracy of this simple semi-empirical equation might be comparable to the performance for dry weather conditions of more sophisticated numerical models (e.g., WRF or uSINGV), which include complex building effect parameterizations.

The present model serves as a reliable and easy-to-use tool to calculate the spatial variability of UHI_{max} intensity across the tropical city of Singapore. However, there is still potential for improvement. Although the spatial performance of the estimated UHI_{max} is consistent with the expected results according to the LCZ classification, the model should also be evaluated at different measurement points from the locations used to build the equation in order to confirm its accuracy across the entire city. Additional improvements might be incorporated for even better performance, e.g., the inclusion of other factors known to influence the UHI, such as local anthropogenic heat fluxes. The latter would particularly improve the estimation of UHI_{max} magnitudes in areas known to have high anthropogenic heat emissions, such as certain industrial estates or commercial centers with dense building configurations and high traffic volumes.

As with all such approaches, the present semi-empirical model is fundamentally restricted by the statistical relationships between parameters established for the present situation. However, the model has descriptive and practical value by providing UHI_{max} maps that are easy to calculate based on a few input variables. The present semi-empirical equation performs best during calm wind conditions, which coincides with maximum UHI development and highest UHI_{max} values. This is an important result as these situations are associated with reduced outdoor thermal comfort and higher health risk. Hence, the resulting maps can be used to investigate less favorable thermal conditions and assess the population vulnerability to a certain temperature excess and thus identify risk levels of a target region [51]. Additionally, the spatial distribution of the modeled UHI_{max} can provide insights for urban planning strategies [52], as well as for designing corresponding mitigation measures according to the land cover and morphology of a location.

Author Contributions: Conceptualization, B.S. and M.R.; Methodology, B.S. and M.R.; Validation, B.S.; Formal analysis, B.S.; Investigation, B.S., M.R., P.P. and A.S.-M.; Data curation, M.R.; Writing—original draft, B.S.; Writing—review & editing, M.R., P.P. and A.S.-M.; Visualization, B.S. and P.P.; Funding acquisition, M.R. All authors have read and agreed to the published version of the manuscript.

Funding: This research was mostly funded by a National University of Singapore research grant (A-0003071-00-00).

Institutional Review Board Statement: Not applicable.

Informed Consent Statement: Not applicable.

Data Availability Statement: Not applicable.

Acknowledgments: The authors would like to thank those that contributed to the measurement campaign and data pre-processing.

Conflicts of Interest: The authors declare no conflict of interest.

Appendix A. Calculation of the Dimensionless Π Variables

Dimensionless variables Π are defined based on the selected meteorological variables:

$$\Pi_i = \mathrm{UHI_{max}}^a \quad T_{a,ref}^b \quad T_{d,ref}^c \quad U_{ref}^d \quad K_{in}^e \tag{A1}$$

where the physical dimensions of the variables are:

$$[\mathrm{K}]^a \quad [\mathrm{K}]^b \quad [\mathrm{K}]^c \quad [\mathrm{m\ s^{-1}}]^d \quad [\mathrm{K\ m\ s^{-1}}]^e \tag{A2}$$

According to the number of physical dimensions, i.e., temperature, length, and time, we obtain the following system of equations:

$$\begin{aligned} a + b + c + d &= 0 \\ d + e &= 0 \\ -d - e &= 0 \end{aligned}$$

From above, we can create two dimensionless groups setting $d = 0$ and $b = 0$, which results in $a = b = 1$ for the first group. For the second group, having $a = 0$ and $b = 0$ yields $d = -e$, and $c = 1$. Therefore, it results in the following dimensionless variables:

$$\Pi_1 = \frac{\mathrm{UHI_{max}}}{T_{a,ref}} \tag{A3}$$

$$\Pi_2 = \frac{K_{in}}{T_{d,ref} \cdot U_{ref}} \tag{A4}$$

References

1. Stewart, I.D. Why should urban heat island researchers study history? *Urban Clim.* **2019**, *30*, 100484. [CrossRef]
2. Oke, T.R.; Mills, G.; Christen, A.; Voogt, J.A. *Urban Climates*; Cambridge University Press: Cambridge, UK, 2017. [CrossRef]
3. Rizwan, A.M.; Dennis, L.Y.; Chunho, L. A review on the generation, determination and mitigation of Urban Heat Island. *J. Environ. Sci.* **2008**, *20*, 120–128. [CrossRef] [PubMed]
4. Steeneveld, G.J.; Koopmans, S.; Heusinkveld, B.; Van Hove, L.; Holtslag, A. Quantifying urban heat island effects and human comfort for cities of variable size and urban morphology in the Netherlands. *J. Geophys. Res. Atmos.* **2011**, *116, D20*. [CrossRef]
5. Schatz, J.; Kucharik, C.J. Seasonality of the urban heat island effect in Madison, Wisconsin. *J. Appl. Meteorol. Climatol.* **2014**, *53*, 2371–2386. [CrossRef]
6. Oke, T.R. The urban energy balance. *Prog. Phys. Geogr.* **1988**, *12*, 471–508. [CrossRef]
7. Oke, T.R. Canyon geometry and the nocturnal urban heat island: Comparison of scale model and field observations. *J. Climatol.* **1981**, *1*, 237–254. [CrossRef]
8. Unger, J. Intra-urban relationship between surface geometry and urban heat island: Review and new approach. *Clim. Res.* **2004**, *27*, 253–264. [CrossRef]
9. Yuan, C.; Chen, L. Mitigating urban heat island effects in high-density cities based on sky-view factor and urban morphological understanding: A study of Hong Kong. *Archit. Sci. Rev.* **2011**, *54*, 305–315. [CrossRef]
10. Zoulia, I.; Santamouris, M.; Dimoudi, A. Monitoring the effect of urban green areas on the heat island in Athens. *Environ. Monit. Assess.* **2009**, *156*, 275–292. [CrossRef]
11. Oliveira, S.; Andrade, H.; Vaz, T. The cooling effect of green spaces as a contribution to the mitigation of urban heat: A case study in Lisbon. *Build. Environ.* **2011**, *46*, 2186–2194. [CrossRef]
12. Konarska, J.; Holmer, B.; Lindberg, F.; Thorsson, S. Influence of vegetation and building geometry on the spatial variations of air temperature and cooling rates in a high-latitude city. *Int. J. Climatol.* **2016**, *36*, 2379–2395. [CrossRef]
13. Freitas, E.D.; Rozoff, C.M.; Cotton, W.R.; Dias, P.L.S. Interactions of an urban heat island and sea-breeze circulations during winter over the metropolitan area of São Paulo, Brazil. *Bound.-Layer Meteorol.* **2007**, *122*, 43–65. [CrossRef]
14. He, B.J.; Ding, L.; Prasad, D. Relationships among local-scale urban morphology, urban ventilation, urban heat island and outdoor thermal comfort under sea breeze influence. *Sustain. Cities Soc.* **2020**, *60*, 102289. [CrossRef]
15. Skarbit, N.; Stewart, I.D.; Unger, J.; Gál, T. Employing an urban meteorological network to monitor air temperature conditions in the 'local climate zones' of Szeged, Hungary. *Int. J. Climatol.* **2017**, *37*, 582–596. [CrossRef]
16. Stewart, I.D. A systematic review and scientific critique of methodology in modern urban heat island literature. *Int. J. Climatol.* **2011**, *31*, 200–217. [CrossRef]
17. Arnds, D.; Böhner, J.; Bechtel, B. Spatio-temporal variance and meteorological drivers of the urban heat island in a European city. *Theor. Appl. Climatol.* **2017**, *128*, 43–61. [CrossRef]

18. Giannaros, T.M.; Melas, D.; Daglis, I.A.; Keramitsoglou, I.; Kourtidis, K. Numerical study of the urban heat island over Athens (Greece) with the WRF model. *Atmos. Environ.* **2013**, *73*, 103–111. [CrossRef]
19. Chen, F.; Yang, X.; Zhu, W. WRF simulations of urban heat island under hot-weather synoptic conditions: The case study of Hangzhou City, China. *Atmos. Res.* **2014**, *138*, 364–377. [CrossRef]
20. Yang, B.; Zhang, Y.; Qian, Y. Simulation of urban climate with high-resolution WRF model: A case study in Nanjing, China. *Asia-Pac. J. Atmos. Sci.* **2012**, *48*, 227–241. [CrossRef]
21. Salamanca, F.; Martilli, A.; Yagüe, C. A numerical study of the Urban Heat Island over Madrid during the DESIREX (2008) campaign with WRF and an evaluation of simple mitigation strategies. *Int. J. Climatol.* **2012**, *32*, 2372–2386. [CrossRef]
22. Gutiérrez, E.; González, J.E.; Martilli, A.; Bornstein, R.; Arend, M. Simulations of a heat-wave event in New York City using a multilayer urban parameterization. *J. Appl. Meteorol. Climatol.* **2015**, *54*, 283–301. [CrossRef]
23. Li, H.; Zhou, Y.; Wang, X.; Zhou, X.; Zhang, H.; Sodoudi, S. Quantifying urban heat island intensity and its physical mechanism using WRF/UCM. *Sci. Total Environ.* **2019**, *650*, 3110–3119. [CrossRef] [PubMed]
24. Kusaka, H.; Chen, F.; Tewari, M.; Dudhia, J.; Gill, D.O.; Duda, M.G.; Wang, W.; Miya, Y. Numerical simulation of urban heat island effect by the WRF model with 4-km grid increment: An inter-comparison study between the urban canopy model and slab model. *J. Meteorol. Soc. Jpn.* **2012**, *90*, 33–45. [CrossRef]
25. Sharma, A.; Fernando, H.J.; Hamlet, A.F.; Hellmann, J.J.; Barlage, M.; Chen, F. Urban meteorological modeling using WRF: A sensitivity study. *Int. J. Climatol.* **2017**, *37*, 1885–1900. [CrossRef]
26. Bottyán, Z.; Unger, J. A multiple linear statistical model for estimating the mean maximum urban heat island. *Theor. Appl. Climatol.* **2003**, *75*, 233–243. [CrossRef]
27. Hoffmann, P.; Krueger, O.; Schlünzen, K.H. A statistical model for the urban heat island and its application to a climate change scenario. *Int. J. Climatol.* **2012**, *32*, 1238–1248. [CrossRef]
28. Straub, A.; Berger, K.; Breitner, S.; Cyrys, J.; Geruschkat, U.; Jacobeit, J.; Kuehlbach, B.; Kusch, T.; Philipp, A.; Schneider, A.; et al. Statistical modelling of spatial patterns of the urban heat island intensity in the urban environment of Augsburg, Germany. *Urban Clim.* **2019**, *29*, 100491. [CrossRef]
29. Gardes, T.; Schoetter, R.; Hidalgo, J.; Long, N.; Marquès, E.; Masson, V. Statistical prediction of the nocturnal urban heat island intensity based on urban morphology and geographical factors—An investigation based on numerical model results for a large ensemble of French cities. *Sci. Total Environ.* **2020**, *737*, 139253. [CrossRef] [PubMed]
30. Buckingham, E. On Physically Similar Systems; Illustrations of the Use of Dimensional Equations. *Phys. Rev.* **1914**, *4*, 345–376. [CrossRef]
31. Hidalgo, J.; Masson, V.; Gimeno, L. Scaling the daytime urban heat island and urban-breeze circulation. *J. Appl. Meteorol. Climatol.* **2010**, *49*, 889–901. [CrossRef]
32. Lee, T.W.; Lee, J.; Wang, Z.H. Scaling of the urban heat island intensity using time-dependent energy balance. *Urban Clim.* **2012**, *2*, 16–24. [CrossRef]
33. Theeuwes, N.E.; Steeneveld, G.J.; Ronda, R.J.; Holtslag, A.A. A diagnostic equation for the daily maximum urban heat island effect for cities in northwestern Europe. *Int. J. Climatol.* **2017**, *37*, 443–454. [CrossRef]
34. Zhang, X.; Steeneveld, G.J.; Zhou, D.; Duan, C.; Holtslag, A.A. A diagnostic equation for the maximum urban heat island effect of a typical Chinese city: A case study for Xi'an. *Build. Environ.* **2019**, *158*, 39–50. [CrossRef]
35. Yao, L.; Yang, X.; Zhu, C.; Jin, T.; Peng, L.L.; Ye, Y. Evaluation of a Diagnostic equation for the daily maximum urban heat island effect. *Procedia Eng.* **2017**, *205*, 2863–2870. [CrossRef]
36. Yang, X.; Yao, L.; Peng, L.L.; Jiang, Z.; Jin, T.; Zhao, L. Evaluation of a diagnostic equation for the daily maximum urban heat island intensity and its application to building energy simulations. *Energy Build.* **2019**, *193*, 160–173. [CrossRef]
37. Chow, W.T.; Roth, M. Temporal dynamics of the urban heat island of Singapore. *Int. J. Climatol. J. R. Meteorol. Soc.* **2006**, *26*, 2243–2260. [CrossRef]
38. Jin, H.; Cui, P.; Wong, N.H.; Ignatius, M. Assessing the effects of urban morphology parameters on microclimate in Singapore to control the urban heat island effect. *Sustainability* **2018**, *10*, 206. [CrossRef]
39. Roth, M.; Sanchez, B.; Li, R.; Velasco, E. Spatial and temporal characteristics of near-surface air temperature across local climate zones in a tropical city. *Int. J. Climatol.* **2022**, *42*, 9730–9752. [CrossRef]
40. Mughal, M.O.; Li, X.X.; Yin, T.; Martilli, A.; Brousse, O.; Dissegna, M.A.; Norford, L.K. High-resolution, multilayer modeling of Singapore's urban climate incorporating local climate zones. *J. Geophys. Res. Atmos.* **2019**, *124*, 7764–7785. [CrossRef]
41. DOS. *Yearbook of Statistics Singapore 2019*; Department of Statistics (DOS), Ministry of Trade & Industry: Singapore, 2019.
42. Stewart, I.D.; Oke, T.R. Local climate zones for urban temperature studies. *Bull. Am. Meteorol. Soc.* **2012**, *93*, 1879–1900. [CrossRef]
43. Gorelick, N.; Hancher, M.; Dixon, M.; Ilyushchenko, S.; Thau, D.; Moore, R. Google Earth Engine: Planetary-scale geospatial analysis for everyone. *Remote Sens. Environ.* **2017**, *202*, 18–27.
44. Demuzere, M.; Bechtel, B.; Mills, G. Global transferability of local climate zone models. *Urban Clim.* **2019**, *27*, 46–63. [CrossRef]
45. Middel, A.; Lukasczyk, J.; Maciejewski, R.; Demuzere, M.; Roth, M. Sky View Factor footprints for urban climate modeling. *Urban Clim.* **2018**, *25*, 120–134. [CrossRef]
46. Simón-Moral, A.; Dipankar, A.; Roth, M.; Sánchez, C.; Velasco, E.; Huang, X.Y. Application of MORUSES single-layer urban canopy model in a tropical city: Results from Singapore. *Q. J. R. Meteorol. Soc.* **2020**, *146*, 576–597. [CrossRef]

47. Li, R. Spatio-Temporal Dynamics of the Urban Heat Island in Singapore. Master's Thesis, Department of Geography, National University of Singapore, Singapore, 2012.
48. Yow, D.M. Urban heat islands: Observations, impacts, and adaptation. *Geogr. Compass* **2007**, *1*, 1227–1251. [CrossRef]
49. Runnalls, K.; Oke, T. Dynamics and controls of the near-surface heat island of Vancouver, British Columbia. *Phys. Geogr.* **2000**, *21*, 283–304. [CrossRef]
50. Sanchez, B.; Roth, M.; Simón-Moral, A.; Martilli, A.; Velasco, E. Assessment of a meteorological mesoscale model's capability to simulate intra-urban thermal variability in a tropical city. *Urban Clim.* **2021**, *40*, 101006. [CrossRef]
51. Zhu, W.; Yuan, C. Urban heat health risk assessment in Singapore to support resilient urban design—By integrating urban heat and the distribution of the elderly population. *Cities* **2023**, *132*, 104103. [CrossRef]
52. Koopmans, S.; Ronda, R.; Steeneveld, G.J.; Holtslag, A.A.; Klein Tank, A.M. Quantifying the effect of different urban planning strategies on heat stress for current and future climates in the agglomeration of The Hague (The Netherlands). *Atmosphere* **2018**, *9*, 353. [CrossRef]